International Journal of Impact Engineering 121 (2018) 63–76

Contents lists available at ScienceDirect

International Journal of Impact Engineering

journal homepage: www.elsevier.com/locate/ijimpeng

A numerical method for dynamic fracture using the extended finite element method with non-nodal enrichment parameters

Iman Asareh[a], Young-Cheol Yoon[b], Jeong-Hoon Song[c,*]

[a] Department of Civil and Environmental Engineering, University of South Carolina, Columbia, SC 29208, USA
[b] Department of Civil Engineering, Myongji College, 356-1 Hongeun-Dong, Seodaemoon-Ku, Seoul 120-776, South Korea
[c] Department of Civil, Environmental, and Architectural Engineering, University of Colorado, Boulder, CO 80309, USA

ARTICLE INFO

Keywords:
Non-nodal extended finite element method
Dynamic fracture
Enrichment parameter
Explicit time integration
Cohesive law

ABSTRACT

A modified extended finite element method (XFEM) for dynamic fracture is presented with a new methodology to construct the XFEM basis for discontinuities. In this method, the enrichment bases are defined to capture the characteristic discontinuities across the interface. The enrichments are vanished outside the element domain so that no blending of the local partition unity is required. The enrichment parameters effectively represent the physics of the discontinuity and are assigned to non-nodal points, which helps to impose Dirichlet boundary conditions on the interface. This feature successfully dissociates the finite element nodes from the extended finite element approximation; it facilitates the treatment of arbitrary crack propagation in explicit methods. The approach is applied to linear three-node triangular elements for element-by-element crack propagation modeling. The proposed method combined with explicit time integration and a cohesive law can successfully predict the dynamic fracture of ductile and brittle materials. Dynamic simulation results in terms of crack path and speed were effectively computed and match the experimental results. Through these numerical examples, the robustness and performance of the method were successfully demonstrated.

1. Introduction

The extended finite element method (XFEM) [1,2] can be viewed as a variation of the generalized finite element method (GFEM) introduced by Melenk and Babuška [3] whereby arbitrary discontinuities such as cracks and shear bands can be modeled without remeshing. One advantage of the XFEM over the GFEM is that it permits the use of local enrichment bases in the finite element (FE) approximation. For the FE convergence, completeness is a necessary condition, i.e. the local approximation must be capable of reproducing given smooth functions, which for elasticity are rigid body motions and constant strain states. However, the local approximation in conventional XFEM focuses only on reproducing the discontinuous functions along with satisfying compatibility condition among enriched and its contiguous elements. Therefore, in many instances, it is not apparent how to be the XFEM convergence rates.

The XFEM exploits the partition of unity framework to adopt various functions as a basis for reproducing the discontinuous fields; step enrichment functions for strong discontinuity [4], asymptotic crack-tip functions for crack tip modeling [1], distance enrichment functions for weak discontinuities [5,6] and hyperbolic tangent enrichment functions for discontinuities in derivatives [7]. Furthermore, The XFEM has successfully been applied to many other applications; cohesive crack models [8,9], evolution of dislocations [10,11] and modeling of grain boundaries [12]. In addition, the XFEM and GFEM provided a crucial insight for meshless methods [13,14] involving the dynamic fracture simulations. Although in these approaches, the extended approximation effectively captures the discontinuity, it may not be able to reproduce the polynomial functions required for completeness.

One of the main challenges arisen in using XFEM is the implementation; to circumvent such difficulties, several alternative approaches have been developed [15–20] to enable robust and efficient failure modeling. In conventional XFEM, the enrichment part generally spreads over the elements contiguous to the enriched element. These element are often called blending elements and should be treated appropriately [21]. For step enrichment functions, the blending regions can be avoided by shifting enrichment techniques introduced by Zi and Belytschko [9]. Furthermore, in conventional XFEM, the enrichment parameters are assigned to element nodes which are often in common among several elements. This feature violates the local description of enrichment part which dramatically facilitates the XFEM implementation. Therefore, it is desirable to have a technique that can define an

* Correspondence author.
E-mail address: jh.song@colorado.edu (J.-H. Song).

https://doi.org/10.1016/j.ijimpeng.2018.06.012
Received 24 March 2018; Received in revised form 24 May 2018; Accepted 11 June 2018
Available online 05 July 2018
0734-743X/ © 2018 Elsevier Ltd. All rights reserved.

enrichment independent from element nodes.

The main objective of the proposed method is to develop a highly efficient XFEM basis but nevertheless quite accurate formulation for discontinuity modeling. The proposed method considers a set of non-nodal points on the interface whereby it can capture the discontinuities in a function and its derivatives across the interface. In this method, the enrichment parameters are selected as *physically-based* quantities associated to the discontinuity of the problem whereby the Dirichlet boundary conditions can be simply imposed on element edges and the surfaces of discontinuity. Moreover, the associated enrichment functions are constructed so that they vanish on element edges. This feature leads to an enrichment fully defined in a local domain, which dramatically simplifies the XFEM implementation. Hence, it is conceivable to think that the proposed method can be an effective scheme for reproducing discontinuities in an XFEM framework.

An outline of the paper is as follows. In Section 2, we shall first review the conventional XFEM, and then describe the new methodology for constructing enrichment functions where the discontinuous displacement field is modeled by non-nodal enrichment parameters. In Section 3, we set up the governing equations and present the weak form and the discretization for the dynamic fracture simulation. Section 4 describes the cohesive law and cohesive crack model. Finally, in Sections 5 and 6, numerical studies and concluding remarks are presented.

2. Enriched displacement fields for discontinuity

Let us consider a two-dimensional domain $\Omega_0 \in R^2$ with its boundary Γ^0 in the reference configuration as shown in Fig. 1. The material and spatial coordinates are respectively denoted by $\mathbf{X}$ and $\mathbf{x}$ with the motion described by $\mathbf{x} = \mathbf{u}(\mathbf{X}, t)$. The current images of Ω_0 and Γ^0 are denoted by Ω and Γ, respectively. The entire boundary Γ^0 is partitioned into either the essential boundary Γ_u^0 or the natural boundary Γ_t^0 such that $\Gamma_u^0 \cap \Gamma_t^0 = \varnothing$ and $\Gamma_u^0 \cup \Gamma_t^0 = \Gamma^0$.

To construct enrichment functions in the XFEM framework, an accurate description of the interface is often useful. The interface, i.e. the crack surface in this study, can be implicitly defined by a set of level set functions as

$$\mathbf{X} \in \Gamma_c^0 \text{ if } f(\mathbf{X}) = 0 \text{ and } g(\mathbf{X}, t) > 0 \tag{1}$$

As shown in Fig. 2, the signed distance function $f(\mathbf{X})$ can be described by

$$f(\mathbf{X}) = \min_{\overline{\mathbf{X}} \in \Gamma_c} \left\| \mathbf{X} - \overline{\mathbf{X}} \right\| \ \text{sign}\left(\mathbf{n}^+ . \left(\overline{\mathbf{X}} - \mathbf{X} \right) \right) \tag{2}$$

where $\overline{\mathbf{X}}$ is the closest point on the interface to $\mathbf{X}$ and $\|.\|$ denotes the Euclidean norm. $g(\mathbf{X}, t)$ is defined such that the crack is enclosed within the subdomain $g(\mathbf{X}, t) \geq 0$ whereas the crack tip is located by $g(\mathbf{X}, t) = 0$. For discretized domains, the evaluation of the implicit function $f(\mathbf{X})$ can be simplified by finite element discretizations and is then defined by

$$f(\mathbf{X}) = \sum_I f_I N_I(\mathbf{X}) \tag{3}$$

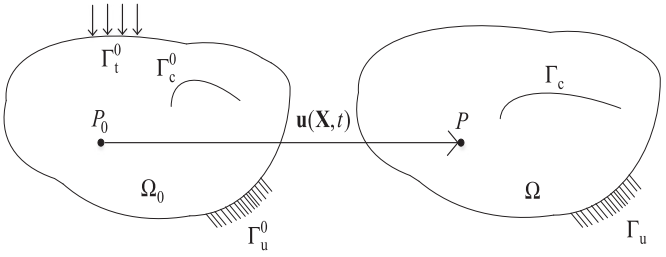

Fig. 1. A two-dimensional domain and its current configuration with a crack.

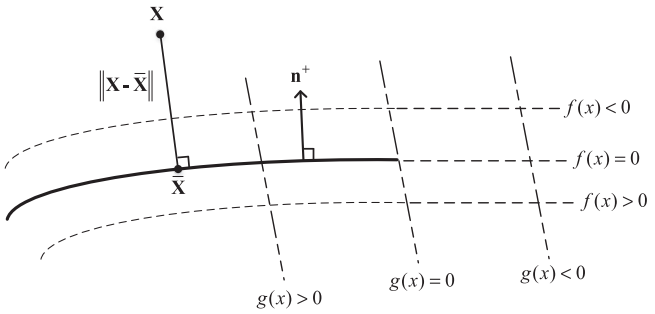

Fig. 2. Crack representation by two level set functions f and g.

Furthermore, the derivatives of the level set functions which are useful in the cohesive force computations can be simply computed by finite element approximations as

$$f(\mathbf{X})_{,i} = \sum_I f_I N_{I,i}(\mathbf{X}) \tag{4}$$

A strong discontinuity in a function, i.e. a displacement jump in crack modeling, can be represented by the Heaviside step function. The Heaviside step function can be also defined in terms of the level set function f given by

$$H(f(\mathbf{X})) = \begin{cases} 0 & f(\mathbf{X}) < 0 \\ 1 & f(\mathbf{X}) > 0 \end{cases} \tag{5}$$

In conventional XFEM, the discontinuous function itself is used as the enrichment function and the partition of unity enables the approximation to reproduce the discontinuous function exactly by satisfying

$$\sum_{I=1}^{n_e} N_I(\mathbf{X}) \Phi(\mathbf{X}) = \Phi(\mathbf{X}) \tag{6}$$

where Φ can be any discontinuous functions. However, in the presented method, the enrichment functions are associated to the non-nodal points and are defined so that they can reproduce the discontinuity without local partition of unity, i.e. the enrichment functions are not multiplied by standard shape functions N_I, and consequently the element nodes are not enriched. In a vector form, the displacement field can then be defined as following:

$$\begin{aligned} \mathbf{u}(\mathbf{X}, t) &= \mathbf{u}^{\text{FEM}}(\mathbf{X}, t) + \mathbf{u}^{\text{ENRICHED}}(\mathbf{X}, t) \\ &= \textstyle\sum_{I=1}^{n_e} N_I(\mathbf{X}) \mathbf{u}_I(t) + \sum_{J \in \delta_{\text{en}}} \Psi_J(\mathbf{X}) \mathbf{a}_J(t) \end{aligned} \tag{7}$$

where δ_{en} is the set of non-nodal enriched points (usually on crack path in two dimensions) and $\mathbf{a}_J$ are the additional degrees of freedom associated with their enrichment function Ψ_J. In the following, first we will describe the crack modeling procedure in two dimensions for a constant strain triangular element, then we will briefly illustrate extending the formulation to both a general discontinuous function and a multi-dimensional multi-node finite element.

2.1. Representation of a crack with non-nodal enrichment parameters for 3-node triangular elements

In this section, we will describe the crack modeling procedure in two dimensions for a constant strain triangular element. We only consider the elements that are completely cut by a crack, i.e., a crack propagates one complete element at a time so that the crack tip is always placed on element edges. Let us consider a finite element with the local node numbers as shown in Fig. 3(a). The crack is assumed to be straight within the element; it has advanced from the surface S_3 to the surface S_1 so that $\mathbf{X}_1^c$ and $\mathbf{X}_2^c$ are the first and second intersection points between the crack and element edges, respectively.

The enrichment variables in crack modeling are considered as jumps

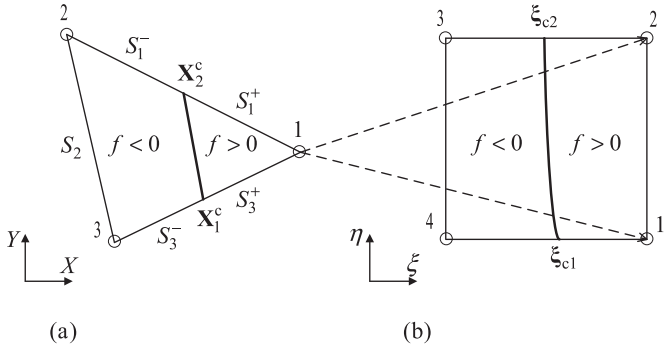

Fig. 3. Duffy's mapping between (a) a triangular element in material coordinates and (b) a biunit square in parent coordinates $-1 \le \xi \le 1;\ -1 \le \eta \le 1$.

in the functions at the non-nodal points; in Fig. 3(a), the jump in displacement at $\mathbf{X}_1^c$ and $\mathbf{X}_2^c$ are denoted by $[[\mathbf{u}]]_1$ and $[[\mathbf{u}]]_2$, respectively. Thus, the approximation is

$$\begin{aligned}\mathbf{u}(\mathbf{X},\ t) &= \sum_{I=1}^{n_e} N_I(\mathbf{X})\mathbf{u}_I(t) + \sum_{J=1}^{2} \Psi_J(\mathbf{X})[[\mathbf{u}(t)]]_J \\ &= \sum_{I=1}^{n_e} N_I(\mathbf{X})\mathbf{u}_I(t) + \Psi_1(\mathbf{X})[[\mathbf{u}(t)]]_1 + \Psi_2(\mathbf{X})[[\mathbf{u}(t)]]_2\end{aligned} \tag{8}$$

where the enrichment variables $[[\mathbf{u}]]_1$ and $[[\mathbf{u}]]_2$ for a scalar component are illustrated in Fig. 4(a).

We construct the enrichment functions so that the approximation in Eq. (8) can reproduce the characteristic function, i.e. the Heaviside step function in Eq. (5). Thus, by substituting the displacement field $\mathbf{u}$ with the vectorized $\mathbf{H}$, Eq. (8) can be rewritten as

$$\mathbf{H}(\mathbf{X},\ t) = \sum_{I=1}^{n_e} N_I(\mathbf{X})\mathbf{H}_I(t) + \Psi_1(\mathbf{X})[[\mathbf{H}(t)]]_1 + \Psi_2(\mathbf{X})[[\mathbf{H}(t)]]_2 \tag{9}$$

For the assumed direction of the crack illustrated in Fig. 3, $\mathbf{H}_1 = 1$, $\mathbf{H}_2 = \mathbf{H}_3 = 0$ and $[[\mathbf{H}]]_{\mathbf{X}\in\Gamma_c} = 1$. Considering $\sum_{I=1}^{n_e} N_I = 1$ and by partitioning Eq. (9) for each side of the interface, we have

$$\begin{aligned}&\Psi_1^+(\mathbf{X}) + \Psi_2^+(\mathbf{X}) = N_2 + N_3 \\ &\Psi_1^-(\mathbf{X}) + \Psi_2^-(\mathbf{X}) = -N_1\end{aligned} \tag{10}$$

It is important to note that finding any sets of enrichment functions that satisfies Eq. (10) enables the extended approximation to reproduce the discontinuous function. However, Eq. (10) does not satisfy the C^0 continuity condition among enriched element and its contiguous elements. Therefore, the enrichment functions are defined to be vanished along specific element edges. For instance, in the first equation, Ψ_1^+ and Ψ_2^+ must vanish along surfaces S_1^+ and S_3^+ as shown in Fig. 3(a), respectively. Thus, we simply assign $\Psi_1^+ = N_3$ and $\Psi_2^+ = N_2$. However in the second equation Ψ_1^- must vanish along both surfaces S_1^- and S_2, and also Ψ_2^- must vanish along surfaces S_3^- and S_2. To facilitate the construction of such enrichment functions, the Duffy transformation which is a mapping from a square to a triangle can be used; the Duffy transformation can be viewed as a mapping from a square in parent coordinates to a triangle in material coordinate as illustrated in Fig. 3. A detailed description of the Duffy transformation can be found in [22–24].

In this transformation, one vertex in the triangle is mapped to an edge in the square. This vertex is chosen such that the crack passes through non-adjacent edges in parent domain. Therefore, this node should be the node opposite to the edge that is not intersected by the crack, which is node 1 here (See Fig. 3(a)). Then, the FE approximation is given by

$$\mathbf{u}(\mathbf{X},\ t) = \sum_{I=1}^{n_e} N_I'(\mathbf{X})\mathbf{u}_I(t) \tag{11}$$

where the Duffy isoparametric shape functions can be expressed in terms of standard bilinear shape functions as

$$\begin{aligned}N_1' &= N_1^{4Q} + N_2^{4Q} \\ N_2' &= N_3^{4Q} \\ N_3' &= N_4^{4Q}\end{aligned} \tag{12}$$

where

$$N_I^{4Q}(\xi,\ \eta) = \frac{1}{4}(1 + \xi_I\xi)(1 + \eta_I\eta) \tag{13}$$

Here, $(\xi_I,\ \eta_I)$ are nodal coordinates of bi-unit square shown in Fig. 3(b). By substituting the shape functions in Eq. (12) into Eq. (10), we can obtain

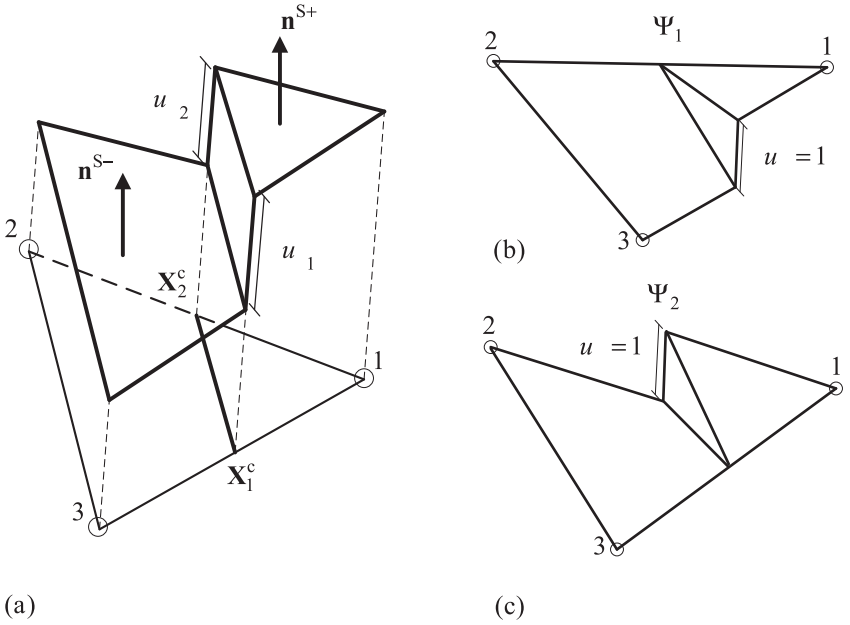

Fig. 4. The enrichment parameters and their associated enrichment functions: (a) the representation of a discontinuity in a two-dimensional model; $\mathbf{n}^{S+}$ and $\mathbf{n}^{S-}$ are normal to the interpolation surfaces; (b) the enrichment function Ψ_1 associated to the non-nodal point $\mathbf{X}_1^c$; and (c) the enrichment function Ψ_2 associated to the non-nodal point $\mathbf{X}_2^c$.

$$\Psi_1^+ + \Psi_2^+ = N_3^{4Q} + N_4^{4Q}$$
$$\Psi_1^- + \Psi_2^- = -N_1^{4Q} - N_2^{4Q} \tag{14}$$

Thus, the C^0 continuity condition is simply satisfied by assigning the enrichment functions as follows

$$\Psi_1 = \begin{cases} -N_1^{4Q} & f < 0 \\ N_4^{4Q} & f > 0 \end{cases}$$
$$\Psi_2 = \begin{cases} -N_2^{4Q} & f < 0 \\ N_3^{4Q} & f > 0 \end{cases} \tag{15}$$

It is important to note that the enrichment functions obtained by the Duffy transformation are in terms of well-known bilinear shape functions. So, one can extensively make use of existing codes for the calculation of the enrichment functions and their derivatives. However, some more code implementation is required to implement the Duffy interpolation.

The enrichment functions in Eq. (15) are shown in Fig. 4(b) and (c). As it can be seen, the enrichment functions have a jump equal to the unity at their associated non-nodal point. The interpolation given in Eq. (8), in addition to the Heaviside step function, can reproduce two planes shown in Fig. 4(a) that their unit normal to the surface of the interpolation are parallel, i.e.

$$\mathbf{n}^{S-} \times \mathbf{n}^{S+} = \mathbf{0} \tag{16}$$

The detailed proof has been provided in Appendix A. However, such a discontinuity modeling is sufficient for failure modeling in homogeneous linear elastic materials since the stresses and strains at both sides of the crack are equal during the failure process due to the fact that both sides of the crack should satisfy traction free condition (or be subjected to equal but in opposite normal cohesive traction). Modeling discontinuity in derivative fields will remain as a future work.

The relations between the bilinear Duffy shape functions and the standard triangle shape functions are obtained in Appendix B. Thus, the enrichment functions can be also expressed in terms of standard shape functions as

$$\Psi_1 = \begin{cases} -\frac{N_1 \times N_3}{N_2 + N_3} & f < 0 \\ N_3 & f > 0 \end{cases}$$
$$\Psi_2 = \begin{cases} -\frac{N_1 \times N_2}{N_2 + N_3} & f < 0 \\ N_2 & f > 0 \end{cases} \tag{17}$$

2.2. General formulations of the non-nodal enrichment XFEM

In this section, we briefly describe the extension of the method for a multi-dimensional multi-node finite element with a general discontinuous function $\Phi(\mathbf{X})$. The discontinuous function is defined as a function of level set function as

$$\Phi(\mathbf{X}) = F(f(\mathbf{X})) \tag{18}$$

As discussed in previous section, Eq. (7) can reproduce the discontinuous function Φ, if it holds for $\mathbf{u} = \Phi$. Thus, Eq. (7) gives

$$\Phi(\mathbf{X}) = \sum_{I=1}^{n_e} N_I(\mathbf{X})\Phi(\mathbf{X}_I) + \sum_{J \in \delta_{en}} \Psi_J(\mathbf{X})\mathbf{a}_J \tag{19}$$

By rewriting Eq. (19) for either side of the interface separately we have

$$\Phi^+(\mathbf{X}) = \sum_{I=1}^{n_e} N_I(\mathbf{X})\Phi(\mathbf{X}_I) + \sum_{J \in \delta_{en}} \Psi_J^+(\mathbf{X})\mathbf{a}_J$$
$$\Phi^-(\mathbf{X}) = \sum_{I=1}^{n_e} N_I(\mathbf{X})\Phi(\mathbf{X}_I) + \sum_{J \in \delta_{en}} \Psi_J^-(\mathbf{X})\mathbf{a}_J \tag{20}$$

The first terms on the right-hand side of Eq. (20) can also be partitioned for sides of the interface as

$$\sum_{I=1}^{n_e} N_I(\mathbf{X})\Phi(\mathbf{X}_I) = \sum_{I \in \delta_n^-} N_I(\mathbf{X})\Phi^-(\mathbf{X}_I) + \sum_{I \in \delta_n^+} N_I(\mathbf{X})\Phi^+(\mathbf{X}_I) \tag{21}$$

where δ_n^+ and δ_n^- are the sets of element nodes that are on the subdomains where $f > 0$ and $f < 0$, respectively.

In this study, we assume that the discontinuous functions at either side of the interface, i.e. Φ^+ and Φ^- are as sufficiently smooth as to be interpolated by standard shape functions. For example, the strong and weak discontinuities are often captured with the Heaviside and distance functions, respectively. This indicates that the enrichment functions are constant or linear on both sides of the interface and therefore, can be exactly interpolated by linear shape functions. So, Φ^+ and Φ^- can be reproduced by finite element shape functions

$$\Phi^+(\mathbf{X}) = \sum_{I=1}^{n_e} N_I(\mathbf{X})\Phi^+(\mathbf{X}_I)$$
$$\Phi^-(\mathbf{X}) = \sum_{I=1}^{n_e} N_I(\mathbf{X})\Phi^-(\mathbf{X}_I) \tag{22}$$

Substituting Eqs. (21) and (22) into (20), we will have

$$\sum_{I \in \delta_n^-} N_I(\mathbf{X})[[\Phi]]_{\mathbf{X}=\mathbf{X}_I} = \sum_{J \in \delta_{en}} \Psi_J^+(\mathbf{X})\mathbf{a}_J$$
$$\sum_{I \in \delta_n^+} -N_I(\mathbf{X})[[\Phi]]_{\mathbf{X}=\mathbf{X}_I} = \sum_{J \in \delta_{en}} \Psi_J^-(\mathbf{X})\mathbf{a}_J \tag{23}$$

where $[[\Phi]]_{\mathbf{X}} = \Phi^+(\mathbf{X}) - \Phi^-(\mathbf{X})$ is the jump in the left and right sides of the enrichment function at $\mathbf{X}$. Note that Eqs. (23) are the key equations used to construct the enrichment functions. It must be stressed that these equations do not suffice to provide closure to the definition of the enrichment functions. In other words, there are no unique enrichment functions and enrichment parameters that satisfy Eqs. (23). The overall procedure to define the enrichments can be organized using the following main steps:

1. Identifying the characteristic function (denoted by Φ here) using a-priori knowledge about the discontinuity in the problem.
2. Introducing the enrichment parameters which are best able to represent the identified discontinuity.
3. Defining the enrichment parameters and their associated enrichment functions so that they satisfy the following conditions:
   (a) Eq. (23).
   (b) The C^0 continuity condition between the enriched element and its contiguous elements.

Note that the enrichment functions for triangular elements obtained in previous section can be simply attained using the aforementioned procedure. As an example, crack modeling in one dimension has been demonstrated in Appendix C.

2.3. Comparison to conventional XFEM

Some methodological issues of the conventional XFEM addressed by the non-nodal enrichment method are briefly described:

- The local partition of unity given in Eq. (6) only builds a partition of unity over reproducing elements for which all element nodes are enriched; see References [21,25–27] for more details. Due to mesh constrains, some of the element nodes may not be enriched for an element completely cut by a crack; these elements are often called blending elements. An example has been depicted in Fig. 5, where a crack has advanced through several elements and the crack tip is on the intersection of elements e_4 and e_5. To satisfy C^0 continuity condition, the nodes placed on the crack tip edge are selected not to be enriched as follows in Fig. 5, which leads to an unenriched node I. Thus, although the crack has crossed over the elements e_1 through e_4, these elements are not still reproducing elements. In contrast to conventional XFEM, in non-nodal enrichment method, the element becomes a reproducing element as soon as the crack passes through it.

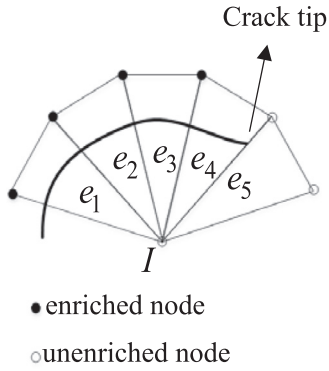

Fig. 5. A crack path on several elements which are not still reproducing elements because the enrichment is not added to node *I*..

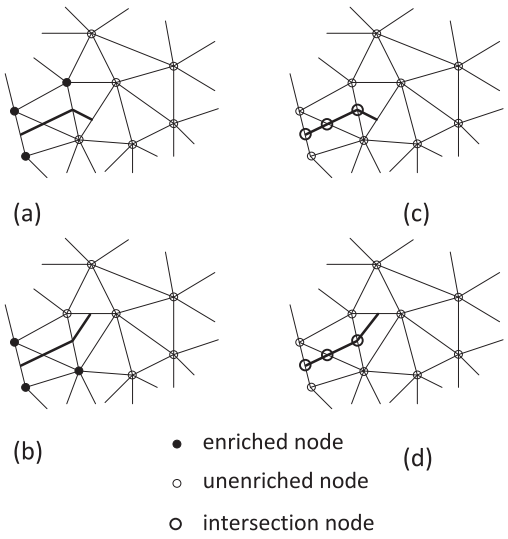

Fig. 6. Selection of enriched nodes: (a)-(b) in the conventional XFEM where enriched nodes are dependent on the direction of crack; and (c)-(d) in the proposed method where the FE nodes are not enriched but an enrichment variable is assigned to each intersection point.

- The conventional XFEM approximations do not, in general, satisfy the Kronecker-δ property that leads to difficulties in imposition of Dirichlet boundary conditions on enriched nodes. As proposed in References [5,9], the Kronecker-δ property can be achieved by shifting enrichment functions with respect to element nodes. However, shifting enrichment functions renders the construction of lumped mass matrix difficult which is crucial for efficient dynamic analysis. In the proposed method, the enrichment functions are vanished on element edges and consequently the Kronecker-δ property is essentially satisfied.
- Although the shifted enrichment functions hold Kronecker-δ property, they may not vanish on parts of element boundaries, and consequently spread over contiguous elements. This may influence the imposition of Dirichlet boundary conditions on element edges. Moreover, to preclude the parasitic terms added to the approximation, the contiguous elements which are often called blending elements are required to be treated appropriately. However, in the proposed method, the enrichment functions are vanished outside the element domains and consequently no blending elements appear.
- In conventional XFEM, the interpretation of the enrichment parameters is difficult so that the non-smooth Dirichlet boundary conditions and interface conditions may not be easily imposed on enrichment parameters. One of the main Dirichlet boundary conditions imposed on the contact interface is impenetrability condition. In non-nodal enrichment method, the impenetrability condition can be easily applied as a Dirichlet boundary condition in the strong form as

$$\text{if}[[\mathbf{u}]] = 0, \quad [[\dot{\mathbf{u}}]].\,\mathbf{n} \geq 0 \tag{24}$$

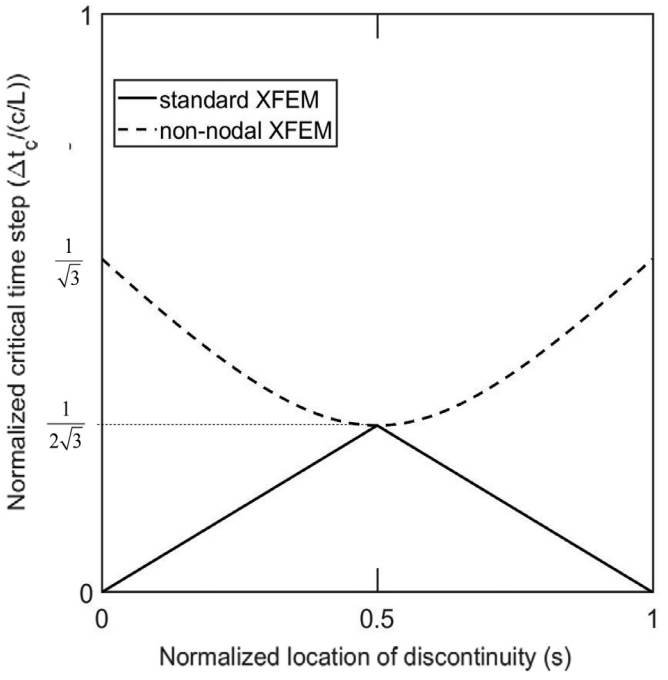

Fig. 7. The variation of normalized critical time step size according to the normalized location of the discontinuity.

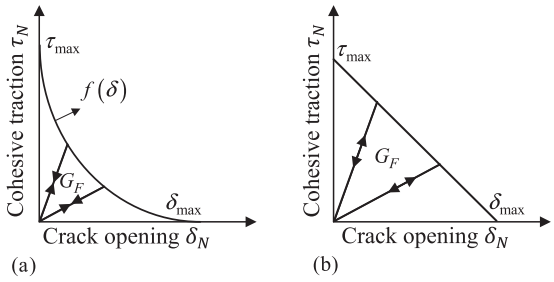

Fig. 8. Cohesive law; the area under the cohesive law curve is the same as the fracture energy (a) a general cohesive law; and (b) a linear cohesive law.

- In the conventional XFEM, the enriched nodes are chosen based on both the direction of the crack growth and whether it is contiguous to an existing crack or not. As shown in Fig. 6(a) and (b), the set of enriched nodes is dependent on the crack directions. However, in the presented method, enriching procedure depends on neither the crack direction nor the elements contiguous to the enriched element which indeed facilitates the crack modeling in an object-oriented program. As shown in Fig. 6(c) and (d), wherever a crack passes over an edge, one enrichment variable assigned to the intersection point is added to the enrichment variable set.

3. Governing equations, weak formulation and discretization

3.1. Governing equations

Considering dynamic form of a two-dimensional problem, the governing equation is

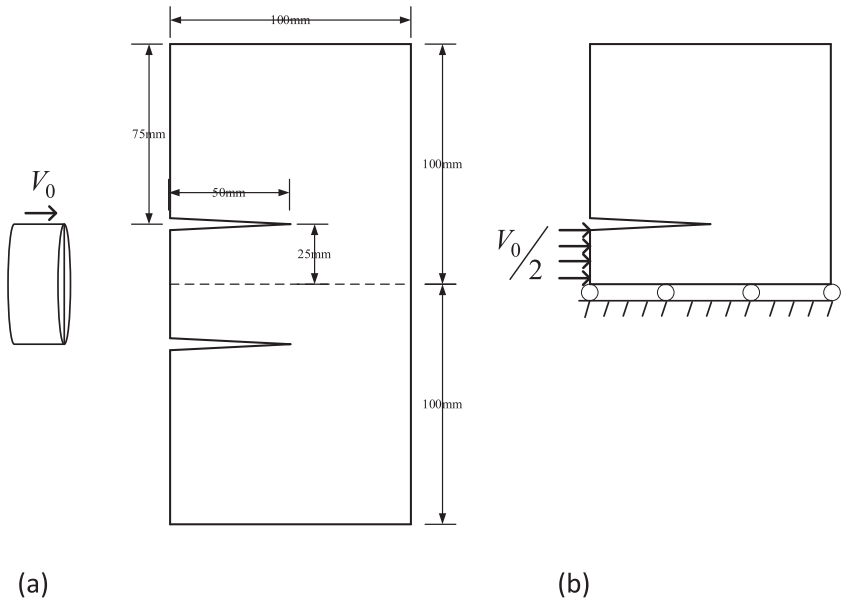

Fig. 9. Experimental set-up and simulation model (a) Kalthoff experimental set-up for crack propagation under impulsive loading (b) Upper half of the plate used in the analysis.

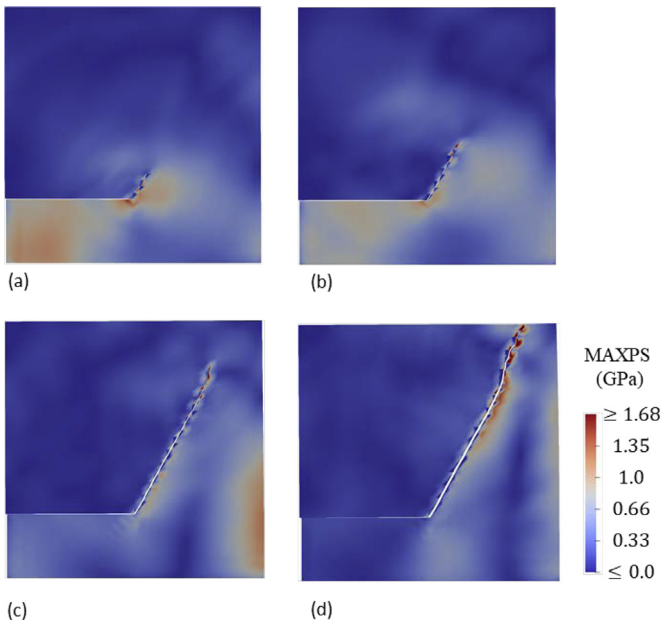

Fig. 10. The computed crack paths on the 40 × 40 deformed mesh with a maximum principle stress at different time steps: (a) $t = 29.89\,\mu s$; (b) $t = 37.43\,\mu s$; (c) $t = 58.48\,\mu s$; and (d) $t = 81.28\,\mu s$.

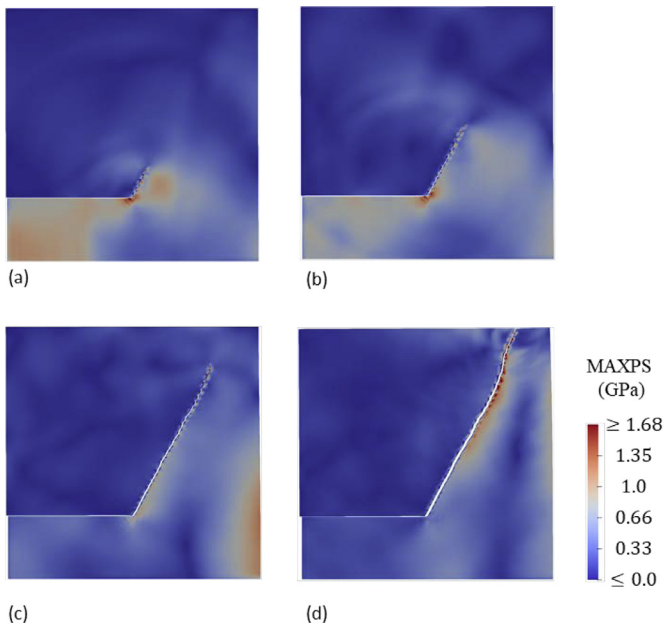

Fig. 11. The computed crack paths on the 80 × 80 deformed mesh with a maximum principle stress at different time steps: (a) $t = 28.83\,\mu s$; (b) $t = 38.09\,\mu s$; (c) $t = 57.0\,\mu s$;and (d) $t = 79.98\,\mu s$.

$$\frac{\partial P_{ji}}{\partial X_j} + \rho_0 b_i - \rho_0 \ddot{u}_i = 0 \quad \text{in } \Omega_0 \tag{25}$$

where **P** is the nominal stress tensor, $\rho_0$is the initial density and **b**is the body force vector per unit mass. The boundary conditions are

$$\begin{aligned} &u_i = \bar{u}_i \quad \text{on } \Gamma_u^0 \\ &[[u]]_j = [[\bar{u}]]_j \quad \text{on } \Gamma_{uc}^0 \\ &n_j^0 P_{ji} = \bar{t}_i^0 \quad \text{on } \Gamma_t^0 \\ &n_j^{0\pm} P_{ji}^{0\pm} = \tau_i^{0c}([[u_i]]) \quad \text{on } \Gamma_c^0 \end{aligned} \tag{26}$$

where $\bar{\mathbf{u}}$ is the applied displacement on the Dirichlet boundary Γ_u^0, $[[\bar{\mathbf{u}}]]$ is the prescribed displacement jump on a set of non-nodal points Γ_{uc}^0, $\bar{\mathbf{t}}^0$ is the applied traction on the Neumann boundary Γ_t^0 and τ^{0c} is the cohesive traction across the crack boundary Γ_c^0. Indicial notation is used for lower case indices. It must be stressed out that a crack tip can be simply modeled by imposing a homogenous boundary condition as

$$[[\mathbf{u}]]_j = 0 \,\text{atcracktip} \tag{27}$$

3.2. Weak formulation

The admissible space for the trial and test functions is defined as follows:

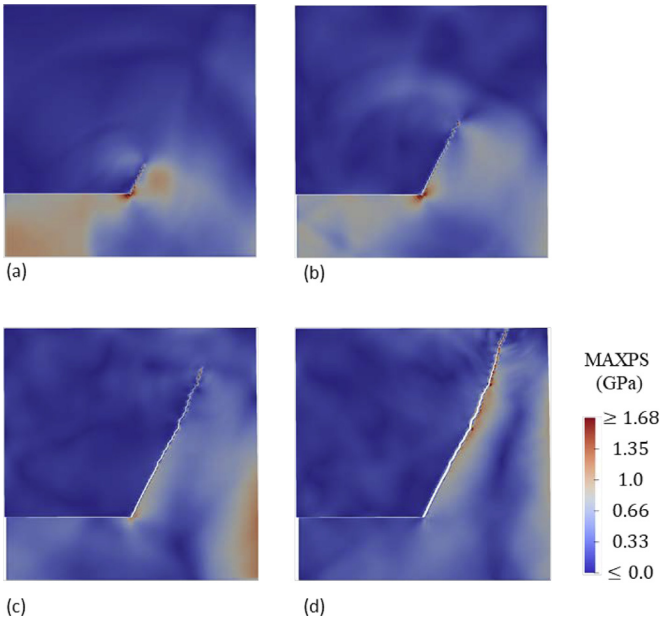

Fig. 12. The computed crack paths on the 120 × 120 deformed mesh with a maximum principle stress at different time steps: (a) $t = 28.96\,\mu s$; (b) $t = 38.45\,\mu s$; (c) $t = 56.49\,\mu s$; and (d) $t = 77.4\,\mu s$.

$$\begin{aligned}&\mathfrak{A} = \{\mathbf{u} \mid \mathbf{u} \in C^0,\ \mathbf{u} = \bar{\mathbf{u}} \text{ on } \Gamma_u^0,\ [[\mathbf{u}]] = [[\bar{\mathbf{u}}]] \text{ on } \Gamma_{uc}^0,\\ &\mathbf{u} \text{ discontinuous on } \Gamma_c\}\\ &\mathfrak{A}_0 = \{\delta\mathbf{u} \mid \delta\mathbf{u} \in C^0,\ \delta\mathbf{u} = 0 \text{ on } \Gamma_u^0,\ \delta[[\mathbf{u}]] = 0 \text{ on } \Gamma_{uc}^0,\\ &\delta\mathbf{u} \text{ discontinuous on } \Gamma_c\}\end{aligned} \tag{28}$$

The weak form is expressed as an integral form of the momentum equation so that for $\mathbf{u} \in \mathfrak{A}$ and $\forall\ \delta\mathbf{u} \in \mathfrak{A}_0$

$$\delta W^{kin} = \delta W^{ext} - \delta W^{int} + \delta W^{coh} \tag{29}$$

where δW^{kin} is the kinetic work, δW^{ext} the external work, δW^{int} the internal work and δW^{coh} the cohesive work achieved by the cohesive traction on the crack surface. The Eq. (29) can be expanded as follows

$$\begin{aligned}\int_{\Omega_0} \delta\mathbf{u}.\,\rho_0\ddot{\mathbf{u}}\mathrm{d}\Omega_0 = &\int_{\Omega_0} \delta\mathbf{u}.\,\rho_0\mathbf{b}\mathrm{d}\Omega_0 + \int_{\Gamma_t^0} \delta\mathbf{u}.\,\bar{\mathbf{t}}^0\mathrm{d}\Gamma_0\\ &- \int_{\Gamma_c} [[\delta\mathbf{u}]].\,\tau^c\mathrm{d}\Gamma_0 - \int_{\Omega_0} \partial\mathbf{F}^T\colon \mathbf{P}\mathrm{d}\Omega_0\end{aligned} \tag{30}$$

where **F** is the deformation gradient.

Table 1
Crack propagation angles and timing data for the Kalthoff's experiment simulations.

Mesh	Angles (°)		Time (μs)	
	Initial	Overall	Propagation	Simulation
40 × 40	60.16	62.45	25.61	81.28
80 × 80	61.87	64.74	22.59	79.98
120 × 120	63.34	67.1	19.79	77.4

3.3. Discretization

The finite element discretization relates each of the virtual work terms in Eq. (29) to a discretized nodal force as follows:

$$\mathbf{f}^{kin} = \mathbf{f}^{ext} - \mathbf{f}^{int} + \mathbf{f}^{coh} \tag{31}$$

where $\mathbf{f}^{kin}$, $\mathbf{f}^{ext}$, $\mathbf{f}^{int}$ and $\mathbf{f}^{coh}$ are the kinematic, external, internal and cohesive forces, respectively. These forces are constructed by assembling the local element force vectors:

$$\mathbf{f}_e^{kin} = \int_{\Omega^e} \rho\mathbf{N}_e^{gT}\mathbf{N}_e^g\mathrm{d}\Omega^e\ddot{\mathbf{d}}_e^g \tag{32}$$

$$\mathbf{f}_e^{ext} = \int_{\Omega^e} \rho\mathbf{N}_e^T\mathbf{b}_e\mathrm{d}\Omega^e + \int_{\Gamma_t^e} \mathbf{N}_e^T\bar{\mathbf{t}}\mathrm{d}\Gamma_t^e \tag{33}$$

$$\mathbf{f}_e^{int} = \int_{\Omega^e} \mathbf{B}_e^{gT}\mathbf{S}_e^g\mathrm{d}\Omega^e \tag{34}$$

$$\mathbf{f}_e^{coh} = -\int_{\Gamma_c^e} [[\Psi]]^T\tau^c\mathbf{n}\mathrm{d}\Gamma_c^e \tag{35}$$

Here the superscript e is the element number, **S** is the second Piola–Kirchhoff stress in Voigt form, $\mathbf{d}_e^g = [\mathbf{u}_e, [[\mathbf{u}]]_J]$ is the generalized nodal coefficient vector consisting of nodal displacements and enrichment variables, $\mathbf{N}_e^g$ is the union of regular shape functions and enrichment functions and $\mathbf{B}_e^g$ is generalized strain-displacement matrix. The $\mathbf{N}_e^g$ matrix is given by

$$\mathbf{N}_e^g = [\mathbf{N}_e^0,\ \Psi_J] \tag{36}$$

The $\mathbf{B}_e^g$ is also given by

$$\mathbf{B}_e^g = [\mathbf{B}_e^0,\ \mathbf{B}_e^c] \tag{37}$$

where

$$\mathbf{B}_I^0 = \begin{bmatrix} N_{I,X}x_{,X} & N_{I,X}y_{,X} \\ N_{I,Y}x_{,Y} & N_{I,Y}y_{,Y} \\ N_{I,X}x_{,Y} + N_{I,Y}x_{,X} & N_{I,X}y_{,Y} + N_{I,Y}y_{,X} \end{bmatrix} \tag{38}$$

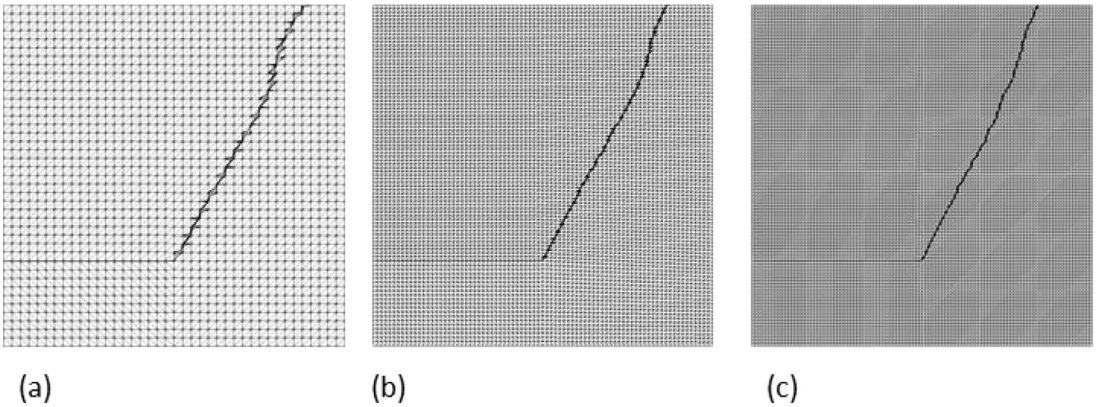

Fig. 13. Comparison of crack propagation trajectories at final simulation step using triangular linear elements (a) 40 × 40 mesh; (b) 80 × 80 mesh; and (c) 120 × 120 mesh.

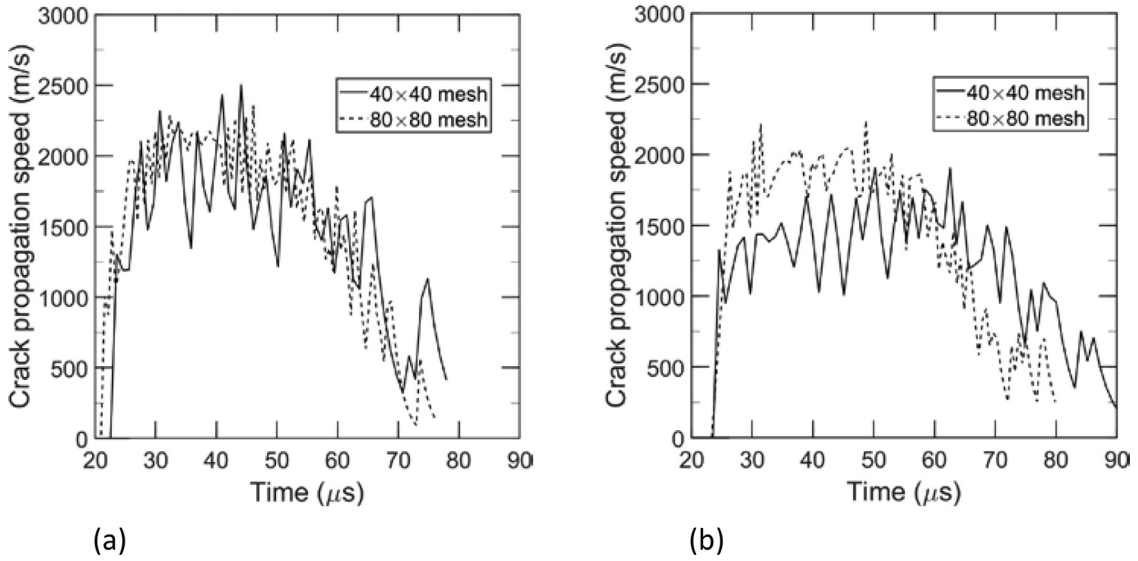

Fig. 14. Crack speeds for the Kolthoff's experiment simulation: (a) the crack speed of this method and (b) the crack speed of the standard XFEM.

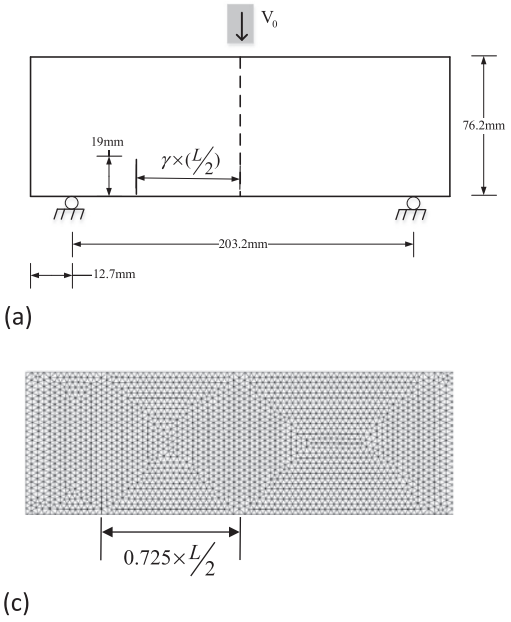

Fig. 15. The geometry and boundary conditions of three-point-bend specimens and finite element meshes used in numerical simulations for the offset notch at the transition point; (a) experiment set-up; (b) a coarse mesh of around 1000 elements; (c) a medium mesh of around 4000 elements and (d) a fine mesh of around 15,000 elements.

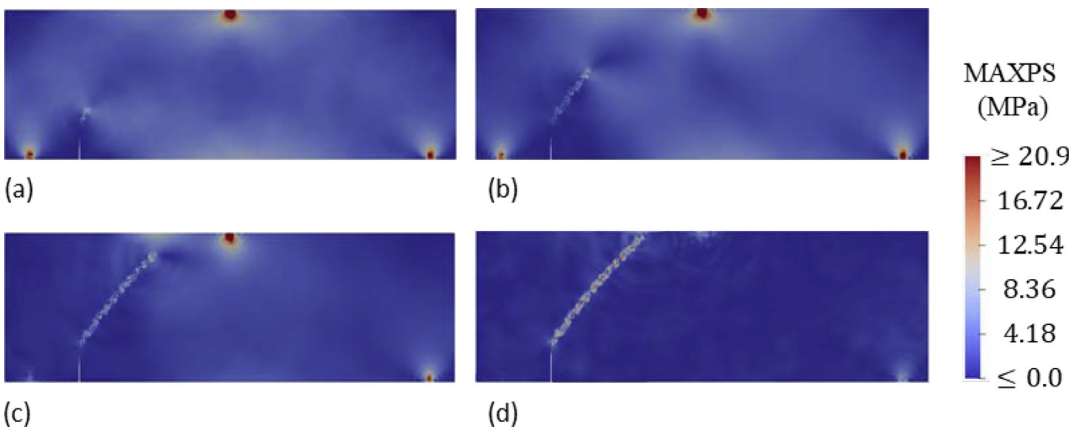

Fig. 16. The computed crack paths for $\gamma = 0.75$ on the fine deformed mesh with a maximum principal stress at different time steps (a) $t = 1142\,\mu s$; (b) $t = 1180\,\mu s$; (c) $t = 1227\,\mu s$; and (d) $t = 1305\,\mu s$.

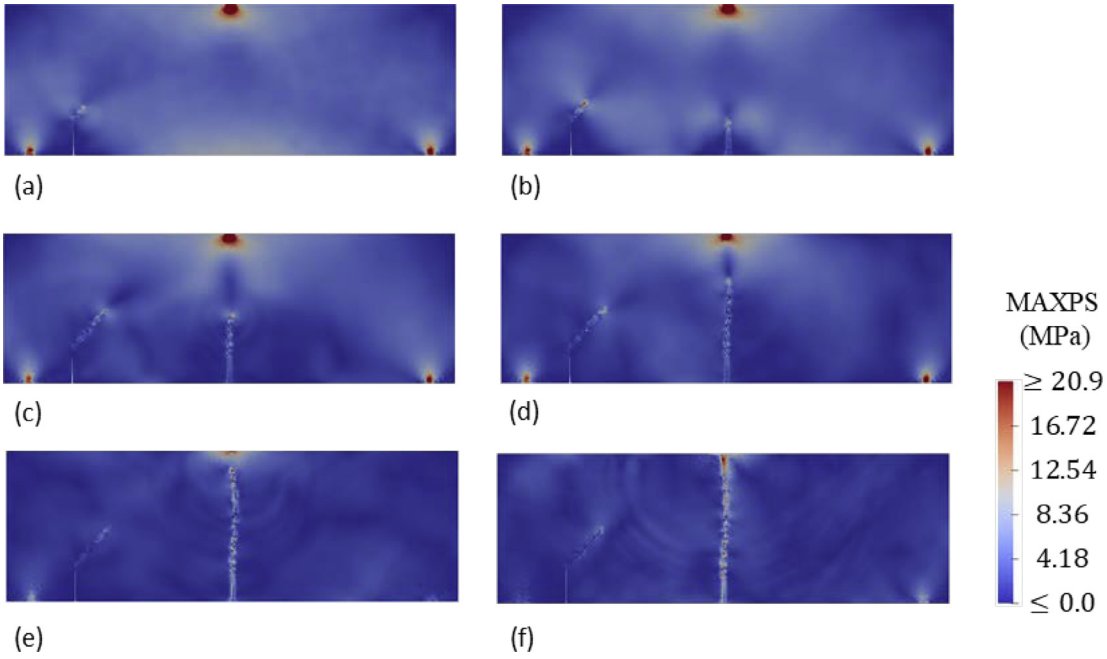

Fig. 17. The computed crack paths for $\gamma = 0.78$ on the fine deformed mesh with a maximum principal stress at different time steps (a) $t = 1329\,\mu s$; (b) $t = 1350\,\mu s$; (c) $t = 1364\,\mu s$; (d) $t = 1385\,\mu s$; (e) $t = 1423\,\mu s$; and (f) $t = 1456\,\mu s$.

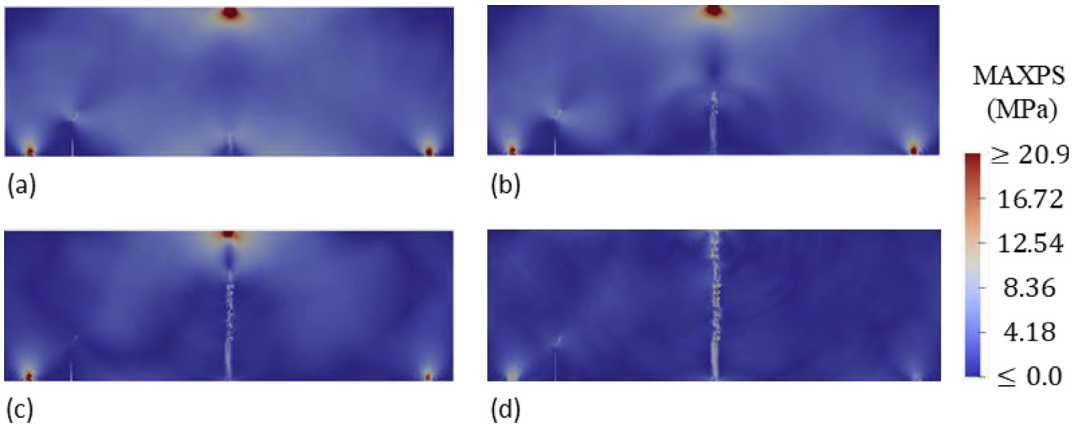

Fig. 18. The computed crack paths for $\gamma = 0.785$ on the fine deformed mesh with a maximum principal stress at different time steps (a) $t = 1316\,\mu s$; (b) $t = 1330\,\mu s$; (c) $t = 1361\,\mu s$; and (d) $t = 1429\,\mu s$.

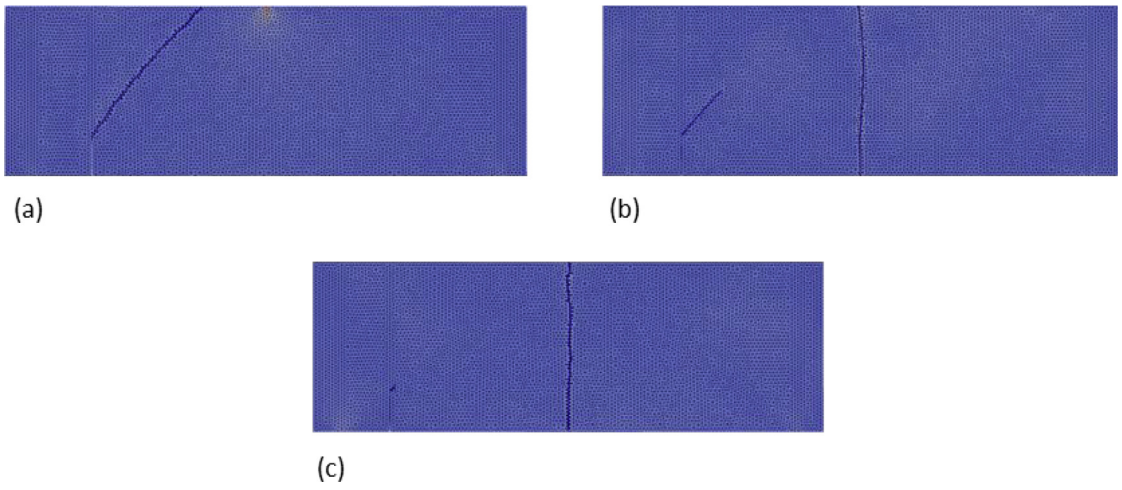

Fig. 19. Fine mesh crack patterns for different offset parameter γ: (a) $\gamma = 0.75$; (b) $\gamma = 0.78$;and (c) $\gamma = 0.785$.

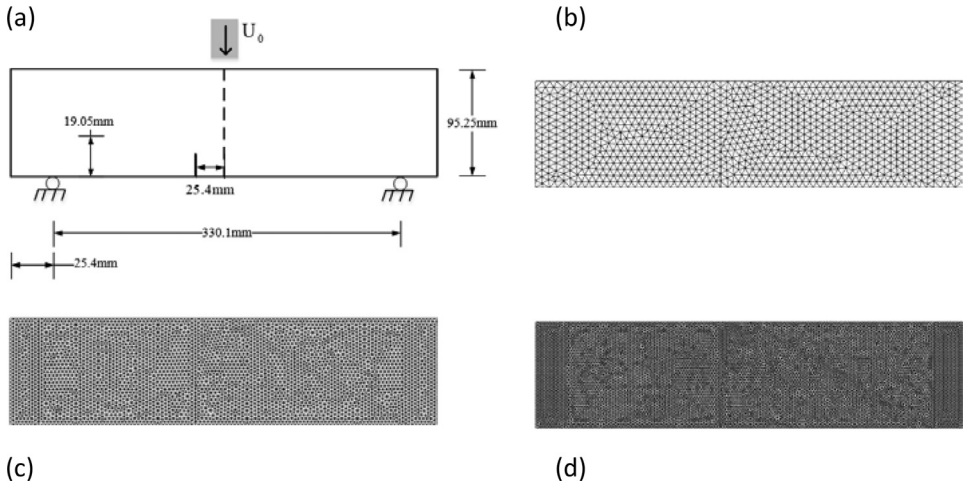

Fig. 20. The geometry and boundary conditions of Guo experiment and finite element meshes used in numerical simulations; (a) experiment set-up; (b) a coarse mesh of around 1100 elements; (c) a medium mesh of around 7700 elements and (d) a fine mesh of around 17,200 elements.

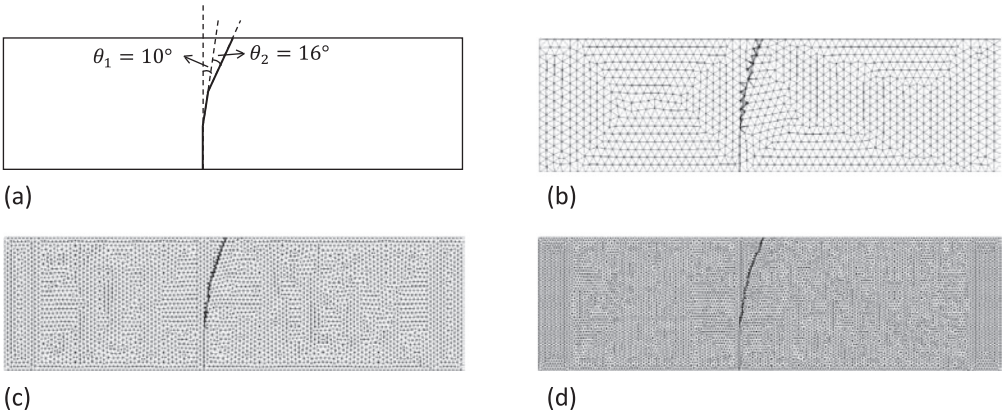

Fig. 21. The crack patterns for different meshes: (a) coarse mesh (b) medium mesh and (c) fine mesh.

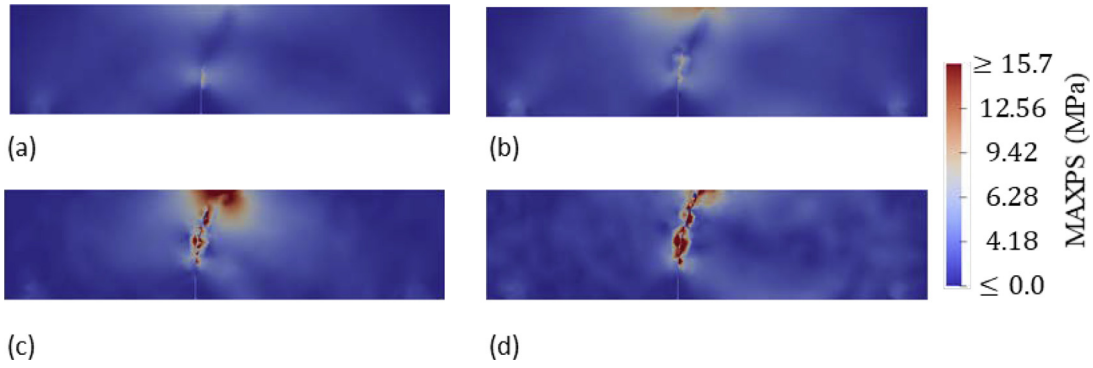

Fig. 22. The crack evolution for the coarse mesh: (a) $t = 370.43\,\mu s$; (b) $t = 531.64\,\mu s$; (c) $t = 607.73\,\mu s$; (d) $t = 742\,\mu s$.

$$\mathbf{B}_I^c = \begin{bmatrix} \Psi_{I,X}x_{,X} & \Psi_{I,X}y_{X} \\ \Psi_{I,Y}x_{,Y} & \Psi_{I,Y}y_{Y} \\ \Psi_{I,X}x_{,Y} + \Psi_{I,Y}x_{,X} & \Psi_{I,X}y_{Y} + \Psi_{I,Y}y_{X} \end{bmatrix} \tag{39}$$

where $(.)_{,i}$ indicates the partial derivative along ith coordinate direction.

3.4. Time integration scheme and critical time step

In this study, the explicit time integration with the consistent mass matrix was used. The explicit time integration is conditionally stable, i.e. it is stable when

$$\Delta t < \Delta t_c = \frac{2}{\omega_{max}} \tag{40}$$

By studying the frequencies ω_i of the one-dimensional discrete system $\omega_i^2 \mathbf{M}\mathbf{d}_i = \mathbf{K}\mathbf{d}_i$, the variation of the critical time step according to the normalized location of the crack was pre-determined to ensure the stability in the explicit time integrator. Fig. 7 compares the normalized critical time step size of the non-nodal XFEM to the standard XFEM.

For the standard XFEM, the peak value of the critical time step size occurs when the crack is at element midspan in contrast to the non-nodal XFEM for which the minimum of the critical time step occurs at the middle. This implies that the non-nodal XFEM is more efficient than

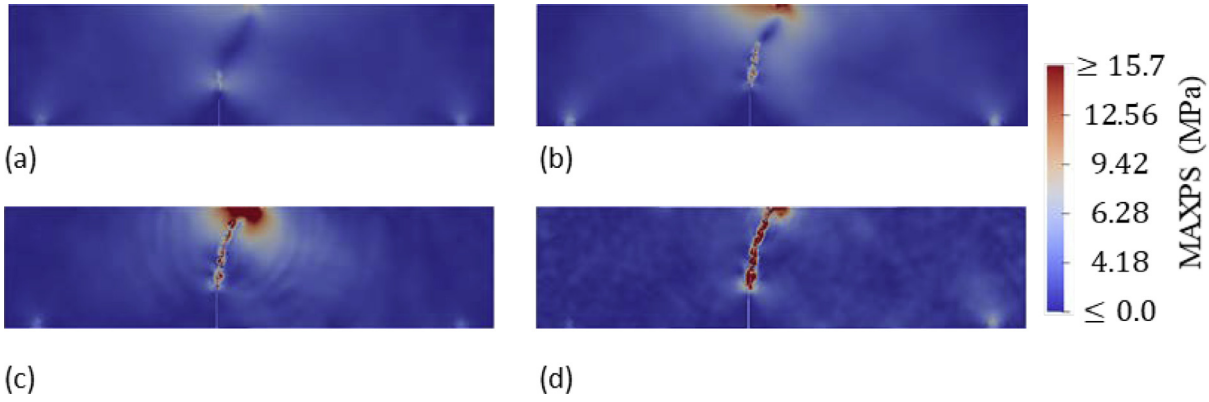

Fig. 23. The crack evolution for the medium mesh: (a) $t = 370.43\,\mu s$; (b) $t = 531.64\,\mu s$; (c) $t = 607.73\,\mu s$; and (d) $t = 742\,\mu s$.

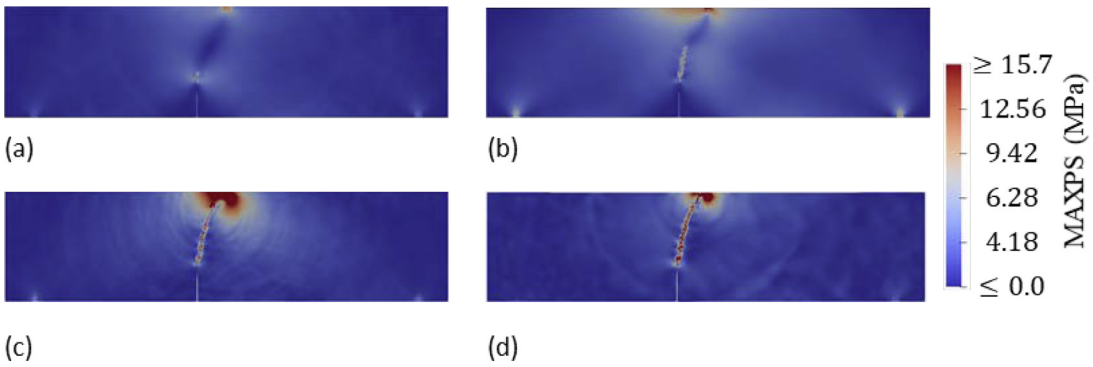

Fig. 24. The crack evolution for the fine mesh: (a) $t = 346.43\,\mu s$; (b) $t = 513\,\mu s$; (c) $t = 616\,\mu s$; and (d) $t = 688\,\mu s$.

Table 2
Crack propagation angles and timing data for the Guo's experiment simulations.

Mesh	Angles (°)		Propagation time μ(s)
	Initial (θ_1)	Final (θ_2)	
Coarse mesh	9.5	11.85	360
Medium mesh	9.0	13.1	319
Fine mesh	10.0	14.0	305

the standard XFEM. Furthermore, for standard XFEM, the critical time step drops linearly to zero as the crack location approaches to the element nodes which leads to numerical difficulties in explicit time integration schemes. However, the critical time steps of the non-nodal XFEM are approached to those obtained for a regular finite element with a consistent mass matrix, when the discontinuity approaches to element nodes. Therefore, the proposed method can be directly used for arbitrary cracks modeling.

4. Cohesive law

The cohesive model is applied to the damage evolution created by the crack. In a cohesive model, a surface traction determined by a cohesive law is applied onto the crack surfaces Γ_c such that the energy dissipated due to the crack evolution matches the critical fracture energy. In this study, we considered only the normal component of the traction. The normal displacement jump δ_N is defined by

$$\delta_N = \mathbf{n}.\,[[\mathbf{u}]] = \mathbf{n}.\sum_{J\in\delta_{\text{en}}} [[\Psi]]_J\,[[\mathbf{u}]]_J \tag{41}$$

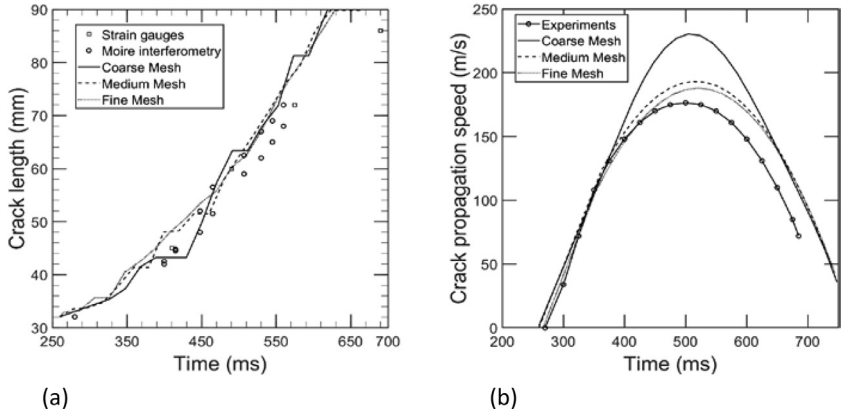

Fig. 25. Crack length history and crack speeds obtained in numerical simulations for different meshes compared to the Guo's experiment: (a) the crack length histories; and (b) the crack speeds.

In general, the cohesive traction can be computed incrementally with radial return algorithm as follows:

input: δ_N
$\delta_N^0 = \delta_N^{\text{prev}}$
$\tau_N^0 = \tau_N^{\text{prev}}$
$E^0 = E^{\text{prev}}$
for $i = 1$ to N
  $\delta_N^i = \delta_N^{i-1} + \frac{i \times \delta_N}{N}$
  if $\delta_N^i > 0$
    $\tau_N^{\text{trial}} = \tau_N^{i-1} + E^{i-1}(\delta_N^i - \delta_N^{i-1})$
    if $\tau_N^{\text{trial}} > f(\delta_N^i)$
      $\tau_N^i = f(\delta_N^i)$
      $E^i = \tau_N^i / \delta_N^i$
return τ_N^i (42)

where δ_N and δ_N^i are the normal displacement and incremental displacement, respectively. In the radial return algorithm, the loop invariant is $E_N = \tau_N^i/\delta_N^i$ while δ_N^i and τ_N^i are underneath the traction law illustrated in Fig. 8.

For the linear cohesive model, we have

$$\delta_{\max} = \frac{2G_F}{\tau_{\max}} \tag{43}$$

In this study, normal cohesive traction is considered only since mode I failure is a dominant failure mode of the subsequently described failure problems.

5. Numerical examples

In this section, we examine the performance of non-nodal XFEM through three benchmark problems for which the experimental results are available. We compare the method with conventional XFEM to effectively demonstrate merits and demerits of the method. We now define notable features that will be used in the numerical simulations that follow. All simulations were modeled with linear triangular elements in plane strain and the thickness was chosen to be unity. The central difference method for time integration is used with a Courant number of 0.1. To advance the crack, the maximum tensile stress computed at the crack tip was considered as fracture criterion along with an element-by-element propagation of the crack. For the crack propagation direction, we used the normal to the maximum tensile stress direction. To eliminate the awkward oscillations in stress computation, once an element failed, a nodal smoothing is performed for the stresses around the crack tip.

5.1. Edge-cracked plate under impulsive loading

The first numerical example deals with an experiment carried out by Kalthoff and Winkler [28] in which a plate with two initial edge notches impacted by a projectile. Numerical results for this problem have been given by Belytschko et al. [29] and Song et al. [30]. Kalthoff observed two different failure modes by modifying the projectile speed V_0; at lower impact velocities, a brittle fracture with a crack propagation at an angle of about 70° was observed while at higher impact velocities, a strain localization, i.e. a shear band was observed at a negative angle of about − 10° with respect to the notch. In this work, we consider only the brittle fracture mode.

Due to twofold symmetry, only the upper half of the plate is modeled. A schematic description of the original problem and the upper part to be solved are shown in Fig. 9(a) and (b), respectively. The symmetry condition $u_y = 0$ was imposed at the bottom edge of the model. The initial velocity is applied as a step function on the left edge on $0 \le y \le 25$ mm. Assuming that the projectile and the plate have identical elastic impedance, an applied velocity of 16.5m/s is chosen, which is one-half of the projectile speed in the experiment.

The plate is a maraging steel 18Ni1900 with the following material parameters: $E = 190$ GPa, $\rho = 8000\text{kg/m}^3$ and $\nu = 0.3$; so, the Rayleigh wave speed is roughly $c_R = 2800\text{m/s}$. The critical stress intensity factor is taken as $K_{Ic} = 68\,\text{MPa}\sqrt{\text{m}}$ which leads to a fracture energy $G_F = 2.217 \times 10^4\text{J/m}^2$. We used a linear cohesive crack model with a tensile strength of $\tau_{\max} = 844$ MPa which corresponds to a critical crack opening displacement $\delta_{\max} = 5.245 \times 10^{-5}$ m. To observe the mesh sensitivity, we have analyzed the model with three different uniform meshes: a 40 × 40 coarse mesh, a 80 × 80 medium mesh and a 120 × 120 fine mesh. The crack evolutions for each mesh are shown in Figs. 10–12.

The finite element meshes and their crack growth trajectories are shown in Fig. 13. The simulations terminated when the crack tip passed the upper boundary; all simulations yielded quite similar crack propagation trajectories which agree quite well with those obtained by the conventional XFEM [29,30]. The numerical results for each simulation are listed in Table 1. The data in Table 1 show that the crack begins to propagate at earlier times with mesh refinement, which leads to a shorter simulation time. For all simulations, the crack first grows primarily along an initial angle, then near the end of the simulation moves a little bit upward.

The initial and the average overall crack propagation angles are increasing with mesh refinement; the overall angle is approaching to the experimental value with mesh refinement as the overall angle of 67.1° in fine mesh compares well with the experimental value of 70°.

The crack tip propagation speeds for 40 × 40 and 80 × 80 meshes computed by both the proposed method and the conventional XFEM are shown in Fig. 14. As it is demonstrated in Fig. 14(a), for both meshes, the proposed method yields very similar crack speeds. When the crack begins to propagate, its speed oscillates around 2000m/s and after around 50 μs, the crack speed slowly decreases up to the end of the simulation. However, for the conventional XFEM, the crack speeds for the fine mesh are obtained significantly higher than for the coarse mesh. These results confirm the previous results in Reference [29]. Therefore, we can conclude that the proposed method demonstrates less mesh dependency than the conventional XFEM.

5.2. Crack pattern in three-point bending specimens with variable offset notch

Experiments concerning mixed mode dynamic crack propagation in three point bending specimens subjected to impact loading were conducted by John and Shah [31]. The numerical solutions for this example can be found in [30,32–35]. The experimental setup is shown in Fig. 15(a). To induce mixed-mode condition, a notch was located at a variable offset from the midspan. In these series of experiments, the crack patterns and crack initiation angles of specimens are examined for the offset notch at various locations. Finally, for several experiments, three crack propagation patterns were reported depending on the location of the notch which can be described by a normalized parameter γ.

$$\gamma = \frac{d_{\text{notch}}}{L/2} \tag{44}$$

where d_{notch} denotes the distance between the midspan and the notch, and L is the distance between the supports. A transition point was observed in the notch location γ_t, where failure changes from a crack growth at the offset notch ($\gamma < \gamma_t$) to a crack growth at the midspan ($\gamma > \gamma_t$). For a narrow transition region where offset parameter is close to γ_t, both notch and midspan cracks initiate and propagate. The experimentally obtained value of γ_t is 0.77.

Material properties are density $\rho = 2400\text{kg/m}^3$, Young's modulus $E = 31.37$ GPa, Poisson's ratio $\nu = 0.2$ and tensile strength of $\tau_{\max} = 10.45$ MPa. A linear cohesive crack model was used with a fracture energy of $G_F = 19.58\text{J/m}^2$ and its corresponding critical crack

opening displacement $\delta_{max} = 3.75 \times 10^{-6}$m. To model the rubber pad between the beam and impact hammer, the velocity boundary condition at the loading point is applied as a ramp function defined by

$$V(t) = \begin{cases} V_0 t/t_{ramp} & t \le t_{ramp} \\ V_0 & t \ge t_{ramp} \end{cases} \quad (45)$$

where $V_0 = 0.06$m/s and $t_{ramp} = 196\,\mu$s. The imposed velocity was calibrated to result in a strain rate of $0.3\,s^{-1}$ at the midspan which was reported in the experiments (see Reference [32]).

Numerical simulations with three different meshes were carried out: a coarse mesh of around 1000 elements, a medium mesh of around 4000 elements and a fine mesh of around 15,000 elements. The finite element meshes are shown in Fig. 15(b)–(d). The numerical experiments were conducted with various offset parameters to capture observed failure patterns. The numerical simulations show that the initial notch location for the transition stage approaches to the experimentally determined value with mesh refinement. As shown in Fig. 15(b)–(d), the γ_t for the fine mesh was obtained as 0.78, which agrees quite well with experimental result of 0.77. The crack propagation paths for each mesh are shown in Figs. 16–18.

The observed three numerical crack patterns for the fine mesh are shown in Fig. 19. As it is shown for $\gamma = 0.75$ the crack propagates only from the offset notch with an angle of 59° which is very close to the experimental value of 60°. At the final stage of crack growth, the crack rotates a little bit toward the loading point which was also reported in experiments. For $\gamma = 0.78$ where the offset notch is in transition zone, two cracks are initiated both at the midspan and the notch and propagate simultaneously, but the final failure occurs at the midspan. Finally, for $\gamma = 0.785$, only one main crack is initiated at the midspan and propagates toward the loading point.

5.3. Crack extension and velocity in three-point bending specimens

In order to compare the crack speeds of the proposed method with those reported in experiments of three-point-bend specimens, we examined an experiment reported by Guo et al. [36]. This experiment has been also numerically modeled by Ruiz et al. [33] in three dimensions. The experimental set-up is shown in Fig. 20(a). The offset notch is located at 25.4 mm from midspan and extended by approximately 13 mm.

The material used in the simulation has the following properties: density $\rho = 2400$kg/m^3, Young's modulus $\rho = 32.3$ GPa and Poisson's ratio $\nu = 0.2$. Since the load-line displacements were reported in experiments, the impact loading can be applied as a prescribed displacement (for more details, refer to References [33,36]). The dynamic tensile strength of 7.75 MPa (2.5 times of tensile strength) is taken as the maximum tensile stress. A linear cohesive crack model was used with fracture energy of $G_F = 120\,$J/m^2. To examine the mesh sensitivity, three different triangular meshes were used in the numerical simulations as illustrated in Fig. 20(b)–(d).

Fig. 21(a) shows the averaged crack path obtained in experiments. The experiments show that, the crack first grows primarily along an initial angle θ_1 measured from vertical line, then after passing half width of the beam, it rotates θ_2 degrees with respect to initial angle toward the loading point. As shown in Fig. 21(a), the experimentally computed values of θ_1 and θ_2 are 10° and 16°, respectively.

The crack patterns and the crack evolutions for three different meshes are shown in Fig. 21(b)–(d) and Figs. 22–24, respectively. The simulation results are listed in Table 2. The outcomes show that the crack starts propagating in an earlier time with mesh refinement. All simulations have similar crack propagation paths. In these simulations, the crack propagation angles θ_1 and θ_2 are in excellent agreement with the experimentally observed value of 10° and 16°, respectively.

The crack length histories and speeds for different meshes are illustrated in Fig. 25. As it can be seen, the crack speed for the coarse mesh was obtained substantially higher than the experimental speed. For the medium and fine meshes, the crack speeds compare well with observed values. This example demonstrates that for the proposed method, a fine mesh may improve the accuracy of the results.

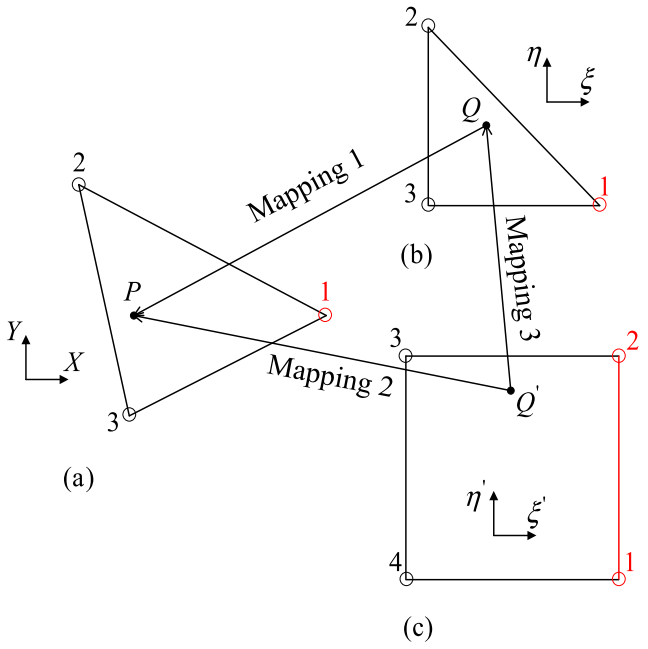

Fig. B1. Mapping among different coordinate systems: (a) physical coordinates; (b) parent coordinate; and (c) Duffy's coordinate. (For interpretation of the references to color in this figure legend, the reader is referred to the web version of this article.)

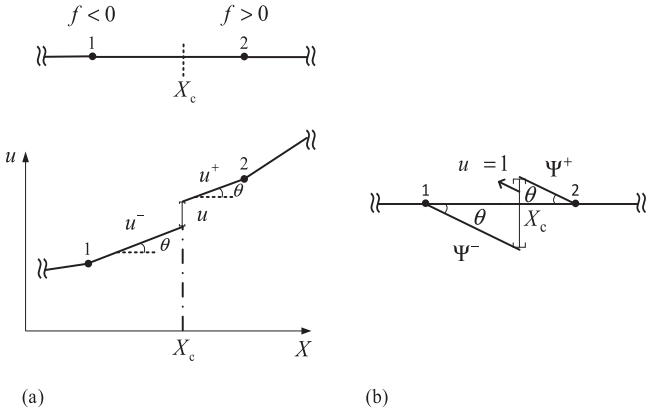

Fig. C1. A strong discontinuity in one dimension: (a) the representation of a discontinuity in a one-dimensional crack model; and (b) one-dimensional crack enrichment function.

6. Conclusions

A new XFEM-based method, which we referred as a non-nodal XFEM, within an explicit time integration scheme has been developed for modeling strong discontinuities in two-dimensional planes. In this method, the discontinuities across an interface are assigned to a set of non-nodal points on the interface. The enrichment variables are defined as *physically-based* quantities and the enrichment functions are defined to be completely vanished outside the element domain. In the proposed method, a local partition of unity is not constructed that excludes the element nodes from the construction of enrichment functions. This feature dramatically simplifies the implementation of the non-nodal

XFEM, unlike the conventional XFEM and its variants including the phantom node method [30,37].

It was demonstrated through three examples that the proposed method can be successfully used in dynamic crack modeling. In the Kalthoff's experiment, this method resulted very similar crack patterns independent of the mesh size. Furthermore, the crack tip speed discrepancy was negligible with mesh refinement, in contrast to conventional XFEM. For mixed-mode crack propagation in three-point-bend specimens, we analyzed the experiments conducted by John and Shah [31] and Guo et al. [36]. In these sequence of numerical experiments, the overall crack propagation paths agreed quite well with those values determined in the experiments. However, in some cases, the crack propagation angles and the crack tip speeds approached to the experiments by mesh refinement. The numerical examples demonstrate that the method can be used for modeling strong discontinuities with the added advantage of excluding the element nodes from extended interpolation.

Finally, we would like to point out that the proposed methodology may be used to model discontinuities in derivatives of a function.

References

[1] Belytschko T, Black T. Elastic crack growth in finite elements with minimal remeshing. Int J Numer Methods Eng 1999;45:601–20.
[2] Dolbow J, Belytschko T. A finite element method for crack growth without remeshing. Int J Numer Methods Eng 1999;46:131–50.
[3] Babuška I, Banerjee U, Osborn JE. On principles for the selection of shape functions for the generalized finite element method. Comput Methods Appl Mech Eng 2002;191:5595–629.
[4] Dolbow J, Moës N, Belytschko T. Discontinuous enrichment in finite elements with a partition of unity method. Finite Elem Anal Des 2000;36:235–60.
[5] Belytschko T, Moës N, Usui S, Parimi C. Arbitrary discontinuities in finite elements. Int J Numer Methods Eng 2001;50:993–1013.
[6] Sukumar N, Chopp D L, Moës N, Belytschko T. Modeling holes and inclusions by level sets in the extended finite-element method. Comput Methods Appl Mech Eng 2001;190:6183–200.
[7] Areias P, Belytschko T. Two-scale shear band evolution by local partition of unity. Int J Numer Methods Eng 2006;66:878–910.
[8] Moës N, Belytschko T. Extended finite element method for cohesive crack growth. Eng Fract Mech 2002;69:813–33.
[9] Zi G, Belytschko T. New crack-tip elements for xfem and applications to cohesive cracks. Int J Numer Methods Eng 2003;57:2221–40.
[10] Gracie R, Oswald J, Belytschko T. On a new extended finite element method for dislocations: core enrichment and nonlinear formulation. J Mech Phys Solids 2008;56:200–14.
[11] Ventura G, Moran B, Belytschko T. Dislocations by partition of unity. Int J Numer Methods Eng 2005;62:1463–87.
[12] Simone A, Duarte C, Van Der Giessen E. A generalized finite element method for polycrystals with discontinuous grain boundaries. Int J Numer Methods Eng 2006;67:1122–45.
[13] Rabczuk T, Song J-H, Belytschko T. Simulations of instability in dynamic fracture by the cracking particles method. Eng Fract Mech 2009;76:730–41.
[14] Ventura G, Xu J, Belytschko T. A vector level set method and new discontinuity approximations for crack growth by Efg. Int J Numer Methods Eng 2002;54:923–44.
[15] Rabczuk T, Belytschko T. Cracking particles: a simplified meshfree method for arbitrary evolving cracks. Int J Numer Methods Eng 2004;61:2316–43.
[16] Rabczuk T, Zi G, Bordas S, Nguyen-Xuan H. A simple and robust three-dimensional cracking-particle method without enrichment. Comput Meth Appl Mech Eng 2010;199:2437–55.
[17] Areias P, Reinoso J, Camanho P, De Sá JC, Rabczuk T. Effective 2d And 3d crack propagation with local mesh refinement and the screened poisson equation. Eng Fract Mech 2017.
[18] Areias P, Rabczuk T. Steiner-point free edge cutting of tetrahedral meshes with applications in fracture. Finite Elem Anal Des 2017;132:27–41.
[19] Areias P, Msekh M, Rabczuk T. Damage and fracture algorithm using the screened poisson equation and local remeshing. Eng Fract Mech 2016;158:116–43.
[20] Areias P, Rabczuk T, Dias-Da-Costa D. Element-wise fracture algorithm based on rotation of edges. Eng Fract Mech 2013;110:113–37.
[21] Chessa J, Wang H, Belytschko T. On the construction of blending elements for local partition of unity enriched finite elements. Int J Numer Methods Eng 2003;57:1015–38.
[22] Duffy MG. Quadrature over a pyramid or cube of integrands with a singularity at a vertex. SIAM J Numer Anal 1982;19:1260–2.
[23] Laborde P, Pommier J, Renard Y, Salaün M. High-order extended finite element method for cracked domains. Int J Numer Methods Eng 2005;64:354–81.
[24] Mousavi S, Sukumar N. Generalized duffy transformation for integrating vertex singularities. Comput Mech 2010;45:127–40.
[25] Fries TP. A corrected XFEM approximation without problems in blending elements. Int J Numer Methods Eng 2008;75:503–32.
[26] Fries T P, Belytschko T. The extended/generalized finite element method: an overview of the method and its applications. Int J Numer Methods Eng 2010;84:253–304.
[27] Ventura G, Gracie R, Belytschko T. Fast integration and weight function blending in the extended finite element method. Int J Numer Methods Eng 2009;77:1–29.
[28] Kalthoff J, Winkler S. Failure mode transition at high rates of shear loading. Dgm Informationsgesellschaft Mbh, Impact Loading And Dynamic Behavior Of Materials. 1. 1988. p. 185–95.
[29] Belytschko T, Chen H, Xu J, Zi G. Dynamic crack propagation based on loss of hyperbolicity and a new discontinuous enrichment. Int J Numer Methods Eng 2003;58:1873–905.
[30] Song J H, Areias P, Belytschko T. A method for dynamic crack and shear band propagation with phantom nodes. Int J Numer Methods Eng 2006;67:868–93.
[31] John R, Shah SP. Mixed-mode fracture of concrete subjected to impact loading. J Struct Eng 1990;116:585–602.
[32] Zi G, Chen H, Xu J, Belytschko T. The extended finite element method for dynamic fractures. Shock Vib 2005;12:9–23.
[33] Ruiz G, Pandolfi A, Ortiz M. Three-dimensional cohesive modeling of dynamic mixed-mode fracture. Int J Numer Methods Eng 2001;52:97–120.
[34] Belytschko T, Organ D, Gerlach C. Element-free Galerkin methods for dynamic fracture in concrete. Comput Meth Appl Mech Eng 2000;187:385–99.
[35] Belytschko T, Tabbara M. Dynamic fracture using element-free Galerkin methods. Int J Numer Methods Eng 1996;39:923–38.
[36] Guo Z, Kobayashi A, Hawkins N. Dynamic mixed mode fracture of concrete. Int J Solids Struct 1995;32:2591–607.
[37] Lua J, Zhang T, Fang E, Song J-H. Explicit phantom paired shell element approach for crack branching and impact damage prediction of aluminum structures. Int J Impact Eng 2016;87:28–43.